Measurement of x-ray emission and thermal transport in near-solid-density plasmas heated by 130 fs laser pulses

B. K. F. Young, B. G. Wilson, D. F. Price, and R. E. Stewart
University of California, Lawrence Livermore National Laboratory, P.O. Box 808, Livermore, California 94551
(Received 22 December 1997; revised manuscript received 29 May 1998)

Near-solid-density plasmas with peak temperatures of 370 ± 50 eV have been generated using a high-contrast ($\approx 10^{-7}$), 400 nm, 130 fs laser pulse of intensity 3×10^{17} W cm^{-2} at the Ultrashort Pulse Laser at Lawrence Livermore National Laboratory. The x-ray-emission spectra from thin tracer layers of germanium, tamped by layers of plastic, were measured as a function of target depth. The results qualitatively agree with calculations based on detailed local thermodynamic equilibrium (LTE) and modified non-LTE spectroscopic opacity models using plasma conditions determined using LASNEX hydrodynamic simulations. No evidence of thermal flux inhibition into the bulk target material was observed. The experiments and detailed simulations are presented. [S1063-651X(98)01710-3]

PACS number(s): 52.70.La, 52.25.Nr, 52.50.Jm, 52.65.−y

I. INTRODUCTION

The recent development of high-power, ultrashort pulse lasers has provided a way to study the physics of solid density matter at high temperatures [1–14]. With 100 fs laser pulses, it is possible for a high-intensity laser beam to interact directly with supercritical density plasmas and heat solid density material to high energy via inverse bremsstrahlung absorption and supersonic thermal conduction on a time scale faster than hydrodynamic expansion can take place. Because of the high density of the plasma created in this way, the ionization and level populations can be close to local thermodynamic equilibrium (LTE) conditions for temperatures approaching 1 kV. The high-energy density plasmas last for a few hundred femtoseconds to a few picoseconds in the simulations. The production of high-energy plasma by supersonic heat conduction over the first 500 Å near the target surface depends on very steep thermal gradients created by the rapid surface heating of a few skin depths by the laser beam. Deeper portions of the target, from a few thousand angstroms to a few micrometers into the bulk, are compressed and heated to temperatures from tens of eV to hundreds of eV by thermal conduction and strong shocks launched from the hot dense surface plasma. These plasmas provide a unique capability to study the opacity and radiative properties of dense, high-temperature plasmas at or near equilibrium in the laboratory.

Previous measurements of buried layer ion velocities heated by short pulse lasers have indicated that 500 eV solid density plasmas are generated at intensities of 3×10^{17} W cm^{-2}, but there have been few systematic measurements of thermal transport and x-ray generation produced by these hot dense plasmas [4]. Nazir *et al.* have observed radiation from high charge states of iron from a thick buried layer heated by a 300 fs laser that shows similarities to a LTE emission spectra [5]. Gauthier *et al.*, Jiang *et al.*, Chen *et al.*, Tuebner *et al.*, and Zigler *et al.* have measured non-LTE *K*-shell x-ray generation from light elements heated by short-pulse lasers [6–14]. These ultrashort-pulse laser produced plasmas are difficult to study spectroscopically due to the limited size of the plasmas (typically target volumes ≈ 1 μm^3), severe temporal and spatial gradients (time scales ≈ 100 fs, plasma scale lengths of few tens of angstroms to 100 Å) typical to these dense plasmas, and strong dependence on laser conditions such as the prepulse, laser polarization, and angle of incidence. As the power level of these high-intensity, ultrashort-pulse lasers increases, the prepulse level and contrast ratio of the leading edge of the incident laser pulse become critically important. Laser intensities as low as 10^{11} W cm^{-2} can either produce an underdense plasma that will interact with the main laser pulse or potentially heat the target causing the surface to melt and ripple or expand, modifying the laser-matter interaction conditions.

This work extends the current understanding of energy transport and the production of solid density plasmas by ultrashort-pulse, high-intensity lasers as these high-density plasmas approach LTE conditions. In this work, the x-ray-emission spectra from germanium ($Z = 32$) tracer layers were measured at varying depths beneath the surface of the laser plasma interaction zone to determine the electron temperature and thermal transport into the near-solid-density plasma. The tamped target design was optimized such that it partially mitigated prepulse effects, minimized temperature and density gradients, and accurately reflected the thermal variation into the target as the thickness of the CH tamper layer over the thin tracer layer was systematically varied as a function of target depth. The spectroscopic results were compared to detailed time-dependent simulations, which included the laser absorption, hydrodynamics, detailed atomic physics, and dense plasma kinetics using LTE and non-LTE ionization codes and tabulated opacity data [15–24]. LASNEX hydrodynamic simulations [15–17] indicate that the bulk of the x-ray emission from the tamped tracer layer occurs for a very short time duration of 300–500 fs full width at half maximum (FWHM) at the peak temperature and near solid density. The calculated space- and time-integrated emission spectra are compared to the measured x-ray-emission spectra. The results are used to characterize the plasma and to test simple heat conduction models. These results represent a

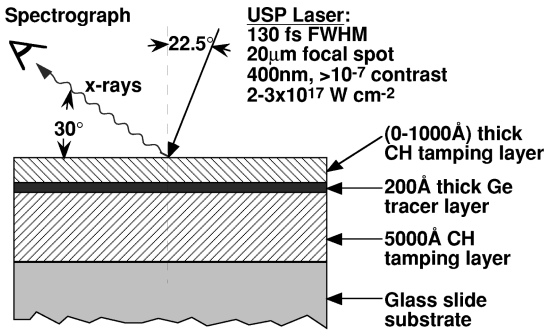

FIG. 1. Schematic of the tamped target composition and typical laser parameters used in these experiments. The Ge target was shot at 3×10^{17} W cm^{-2} and consisted of a 200 Å layer of Ge tamped by 0–1000 Å of CH.

systematic spectroscopic study of heat conduction and high-atomic-number x-ray emission in an ultrashort pulse, laser produced solid-density plasma.

II. EXPERIMENTAL TECHNIQUE

The experiments reported here were conducted at the Ultrashort Pulse Laser (USP) Facility at Lawrence Livermore National Laboratory [4,23–26]. The experiments were conducted at laser intensities of 3×10^{17} W cm^{-2}, at which the 10^{-7} contrast ratio (calculated from the measured 800 nm wave form 1 ps before the peak of the laser pulse) was sufficient to suppress any significant preheat of the target. The 100 fs laser absorption up to intensities $\approx10^{18}$ W cm^{-2} have been successfully measured and modeled [24]. The Ge targets consisted of a 200 Å thick layer of germanium vapor plated onto a glass microscope slide that had been previously coated with 5000 Å of parylene-*n* (CH, $\rho\approx1.1$ g cm^{-3}). This bottom layer of CH helped isolate the emitting plasma from the glass slide, which contained a small percentage of heavy elements that might ionize and emit in the x-ray-emission region of interest for this study (1–2 keV). A schematic of the tamped Ge target is shown in Fig. 1. The Ge tracer layer was then overcoated with a CH tamper layer 0 Å, 100 Å, 500 Å, or 1000 Å in thickness. The measured 0 Å CH/Ge and 100 Å CH/Ge spectra were virtually identical in intensity and spectral content to each other, lending additional evidence of minimal prepulse and preheat of the target.

A great deal of effort was placed in characterizing the USP laser. In particular, the laser prepulse could preheat the target and cause early time target expansion introducing additional spatial or temporal gradients. To minimize the effect, an adjustable pulse stretcher was used to correct third-order phase distortions and harmonically converted light at 400 nm was used to maximize the heating laser contrast [25,26]. The temporal pulse width at 800 nm was determined using a high-dynamic-range second-order scanning autocorrelator. Single-shot third-order autocorrelations monitored shot-to-shot variations in the laser pulse width. The 400 nm laser pulse width was calculated (from the measured 800 nm pulse width) to be 130 fs FWHM for these experiments. The laser energy was monitored using calorimeters at both 800 nm and 400 nm. For these experiments, typically 120 mJ of laser energy was focused to a roughly $18-20$ μm FWHM spot using an $f/3$ off-axis paraboloid away from best focus on the converging side of the beam. *S*-polarized light was used at an angle of incidence 22.5° from normal to the target. Images of the laser focal spot were recorded and characterized. In general, 70% of the laser light was incident on target in a uniform intensity distribution with a $17-18$ μm diameter for the Ge experiments. The ''root mean square'' intensity variation across the spot was less than a factor of 3 for Ge. The peak laser intensity for these experiments was 3×10^{17} W cm^{-2}.

The optical spot size was measured at low intensities by collecting the specularly reflected light off a reference target into the off-axis paraboloid and relaying it into an equivalent plane imaging system. These measurements have been verified using a knife edge to occlude the focal spot at high laser intensities. Additionally, the x-ray-emission spot size was measured using a high-magnification, knife-edge imaging system. A *K*-edge filtered microchannel plate (MCP) intensified detector, with a charged-coupled device (CCD) camera collected the imaged x rays emitted primarily from the tamped germanium plasma [27,28]. The x-ray spot size (for x rays typically over 1 keV transmitted through 25 μm of Be, but less than 5 keV due to the falloff in the detector efficiency of the CsI coated MCP) was determined by differentiating the spatially integrated signal imaged by a gold plated knife edge [28–30]. The overall magnification of the system was approximately 20 with a resolution of better than 5 μm. More heavily filtered channels (12 μm Ti or 6 μm Ni) showed smaller emission spots, although the reduced signal levels did not allow for an accurate spot size measurement. These x-ray spot size measurements are in good agreement with the $\approx18-20$ μm FWHM optical measurements of the laser focal spot size, especially for the 500 Å and 1000 Å thick CH tamped targets. The x-ray spot size probably appears larger near the surface due to the nonlinear variation of the x-ray generation rate with intensity across the focal spot.

The Ge *L*-shell x-ray spectra between 1200 and 1800 eV were measured using a MCP intensified, flat thallium acid phthalate crystal spectrometer. The readout for the spectrometer was a 1024×1024 fiber-optic CCD camera providing single-shot, time- and spatially integrated data [27]. The spectrometer utilized a pair of strong (a few kG/cm) magnets at the entrance window to deflect any fast charged particles away from the diffraction crystal and MCP detector. The spectrometer body was lined with plastic to minimize fluorescence from hard x rays. A Be filter was placed between the diffraction crystal and MCP detector to reduce the ultraviolet and soft-x-ray background level. The MCP and fiber-optic faceplate also acted as a hard-x-ray (>5 keV) filter for the CCD camera itself. The CCD cameras provided nearly instant access to the recorded data, allowing near-real time adjustments in varying the coverage, exposure level, or changes in the laser conditions incident onto the target. The data were stored in their digitized format and the instrumental response including the crystal reflectivity, CsI photocathode, and filter transmission were readily accounted for [28–31].

The measured emission spectra from the USP laser-heated 200 Å thick Ge tracer layer for the three buried layer depths of 100 Å, 500 Å, and 1000 Å are shown in Fig. 2. The

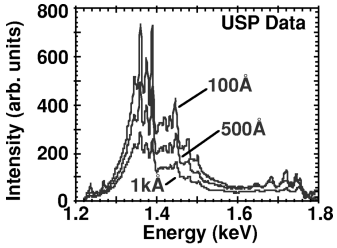

FIG. 2. Space- and time-integrated Ge L-shell emission spectra measured from a 200 Å thick tracer layer tamped by 100 Å, 500 Å, and 1000 Å of plastic.

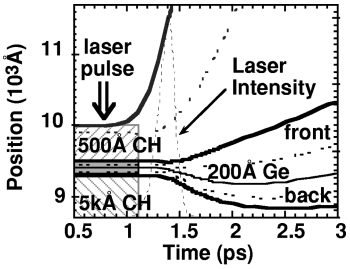

FIG. 3. Time evolution of a 1D LASNEX hydrodynamic grid structure for the 500 Å buried layer target (position in units of 10^3 Å). The USP laser pulse is also shown peaking at 1.4 ps (light dashed line).

data shown represent the average of at least four shots under similar laser conditions with the laser energy and pulse width varying by less than 10%. The spectral coverage included the region from the Ne-like $3s$-$2p$ lines at 1238.6 and 1270.3 eV to the $4d$-$2p$ lines at 1721.0 and 1751.4 eV [32]. The 4-2 transitions appeared to be more isolated than the corresponding 3-2 transitions and may be used as a plasma diagnostic in future experiments [33]. The broadness of the spectral features seen in the data distinguishes it from those seen in conventional laser plasma experiments and are characteristic of a very dense plasma emitter close to local thermodynamic equilibrium [32–35]. The small intensity of the $2p$-$3s$ lines relative to the $2p$-$3d$ and $2s$-$3p$ features in the spectra are also characteristic of a very dense plasma emitter with electron densities above 10^{22} cm^{-3}.

III. DESCRIPTION OF LASNEX HYDRODYNAMIC SIMULATIONS AND THE STA, NON-LTE PHYSICS MODEL

Detailed, numerical simulations of the laser absorption and hydrodynamics were calculated using the LASNEX hydrodynamics calculation package in a one-dimensional Lagrangian planar geometry [15–17]. The simulation solves the Helmholtz wave equation for the laser electromagnetic field by using the ac electrical conductivity model for the target material in the time-dependent calculations as described by Price *et al.* [17,24,36]. The LASNEX calculation used inverse bremsstrahlung absorption based on a complex ac conductivity as the principle laser-target interaction process. Pondermotive effects that couple the laser field to the hydrodynamics were also included. Suprathermal electrons were not included in these calculations [4]. Measurements of x-ray yields at these plasma conditions show very low levels (less than 0.01% of the laser energy on target) of suprathermal electron generation [37]. Heat flow was calculated as electron thermal conductivity without anomalous inhibition or modification, thus limiting the maximum achieved temperature and reducing the duration time of the peak plasma temperature [17,38,39]. The thermal flux limiter was optimized ranging from 0.03 to 1.0 to determine its effect on the calculated heat transport into the target. A discussion of this flux limiter study is presented in Sec. VIII. For the bulk of the simulations used in this work, the thermal transport was described as classical heat conduction using a flux limiter of 1.0.

Both LTE and non-LTE atomic physics packages have been used. For the LTE simulations, the ionic charge state distribution was governed by the Saha distribution and the ionization temperature T_z was the same as the electron temperature T_e. For the non-LTE case, LASNEX invoked a relatively simple time-dependent, average atom model such as XSN (XSN is a non-LTE emission/absorption coefficient code subroutine) or a slightly more sophisticated statistical configuration accounting (SCA) model [17,40,41]. The detailed atomic physics was included using a slight modification of Busquet's [20,23] on-line approach. In Busquet's RADIOM code, non-LTE emission and absorption coefficients were approximately synthesized from tabulated LTE opacity data. For plasma regimes with a Maxwellian electron distribution at temperature T_e, but with a non-Planckian photon distribution, Busquet's model defined an ''ionization temperature'' T_z such that the average ionization stage in LTE reproduced the correct non-LTE mean ionization, $\langle Z_{NLTE}(T_e)\rangle = \langle Z_{LTE}(T_z)\rangle$. The total non-LTE opacity (including stimulated emission corrections) was then constructed from the LTE tabulated free-free coefficient, taken at the actual electron temperature T_e, and the LTE tabulated bound-bound and bound-free coefficient, taken at the effective ionization temperature T_z. A modified treatment, developed by Zimmerman and implemented in LASNEX for these simulations, did not require the separate tabulation of LTE free-free absorption coefficients [42]. A more detailed discussion of this method is presented in Ref. [23]. The tabulated LTE opacities were generated by the STA code of Bar-Shalom *et al.* [18,19] and values of the ionization temperature were obtained by matching the LTE XSN mean ionization to that given by the non-LTE XSN. The resulting ''non-LTE'' STA LASNEX package provides an improved spectral emission predictive modeling capability in conjunction with the radiative hydrodynamics for high-density, LTE, and non-LTE plasmas [21–23].

IV. GERMANIUM LASNEX SIMULATIONS

Detailed LASNEX hydrodynamic simulations for tamped Ge targets were performed using a thermal flux limiter of 1.0. A flux limiter of 1.0 matches previous results for similar plasmas [4] and is discussed in further detail in Sec. VIII. The evolution of the short-pulse, laser-heated tamped target is illustrated by considering the one-dimensional LASNEX hydrodynamic grid for the 500 Å CH case as a function of time shown in Fig. 3. As the laser energy is absorbed, the plastic overcoat decompresses while the 200 Å thick Ge tracer layer remains well tamped during the USP laser heating pulse, expanding by approximately a factor of 5 in volume 1 ps

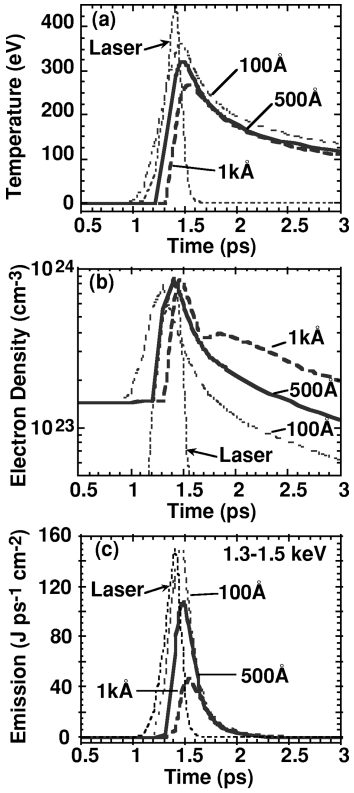

FIG. 4. (a) LASNEX non-LTE STA electron temperature (eV) profiles for the three buried layer target thicknesses, 100 Å (light dotted line), 500 Å (heavy solid line), and 1000 Å (heavy dashed line); (b) predicted electron density profiles (cm^{-3}); (c) calculated time history of the 1.3–1.5 keV x-ray-emission fluence ($J\,ps^{-1}\,cm^{-2}$).

later. The time histories for the electron temperature and density at the middle of the 200 Å thick Ge tracer layer and the integrated x-ray-emission spectra between 1.3 and 1.5 keV are shown in Fig. 4. The LASNEX simulations indicate very short emission times (roughly 300 fs FWHM trailing the peak of the USP laser pulse by less than 100 fs), due to modest decompression of the Ge tracer layer and cooling on expansion. The bulk of the calculated space- and time-integrated x-ray emission from the tamped Ge tracer layer is derived from solid-density plasmas at peak electron temperatures of 250–350 eV. The ''afterglow'' contribution to the measured emission from the underdense, lower-temperature plasma is minimal. The time histories of the mean charge state distributions for both the LTE and non-LTE STA simulations are shown in Fig. 5. The LTE charge state distribution peaks at a slightly higher ionization level (+21 at 500 Å) than in the non-LTE case (+19).

The LASNEX simulations predicted the 200 Å thick Ge tracer layer would remain reasonably isotropic for approximately 1 ps (centered on the peak of the laser pulse) when tamped by 500 Å to 1000 Å of CH. During the short x-ray-emission time, the 200 Å thick Ge tracer layer remained at solid density and roughly in a 50 eV temperature range centered at 330 and 260 eV for the 500 Å and 1000 Å tamping thicknesses, respectively. Furthermore, the mean ionization distribution for either the LTE or non-LTE cases varied by two to three charge states, across the entire 200 Å tracer layer thickness. In general, targets tamped by only 100 Å of CH exhibited temperature and density gradients and ionization variations 3–5 times as great as the more heavily tamped cases. Therefore, 500–1000 Å of plastic appears to have adequately tamped the 200 Å Ge tracer layer at these laser intensities and maintained reasonably isotropic plasma conditions that were critically important for comparisons of these time- and spatially integrated measurements to detailed LASNEX simulations.

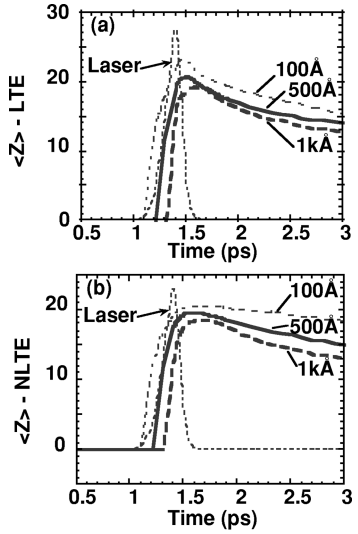

FIG. 5. (a) Time dependence of the mean LASNEX LTE charge state $\langle Z \rangle$ for the tamped Ge buried layer for the three buried layer target thicknesses, 100 Å (light dotted line), 500 Å (heavy solid line), and 1000 Å (heavy dashed line); (b) time dependence of the mean LASNEX non-LTE Ge ionization distribution.

V. COMPARISON OF MEASURED SPECTRA WITH CALCULATED SPECTRA

The measured L-shell emission spectra from the USP laser-heated 200 Å thick Ge tracer layer for the three buried layer depths of 100 Å, 500 Å, and 1000 Å are shown in Fig. 2. The overall emission output dropped as the Ge tracer layer was more deeply tamped as might have been expected due to a temperature gradient into the target and the short emission times for near-solid-density plasmas. The LASNEX spectral simulations employing LTE and non-LTE ionization physics and using the average atom XSN model [40,41] or the SCA model [17] are shown in Fig. 6(a). The XSN and SCA simulations appear as broad, featureless spectra that generally predict the ionization physics of the problem but clearly do not have sufficient detail to accurately describe the spectral data. The XSN and SCA simulations were for semi-infinite slabs of Ge and not the buried layer Ge targets used in the experiment or other simulations presented in this paper. LASNEX simulations using the current LTE and non-LTE STA [18,19] emission models utilizing STA opacity data are shown in Figs. 6(b) and 6(c) and are in better qualitative agreement with measured data. The falloff in the relative emission output with tamping depth is similar to that of the measured spectra and indicates that the calculated temperature gradient into the target and approximate ionization distribution may be consistent with the experiment. The calculated peak temperatures ranged from 350 to 400 eV near the surface ($\approx$200 Å) decreasing to 250–300 eV at 1000 Å into the target at a laser intensity of 3×10^{17} $W\,cm^{-2}$. All cal-

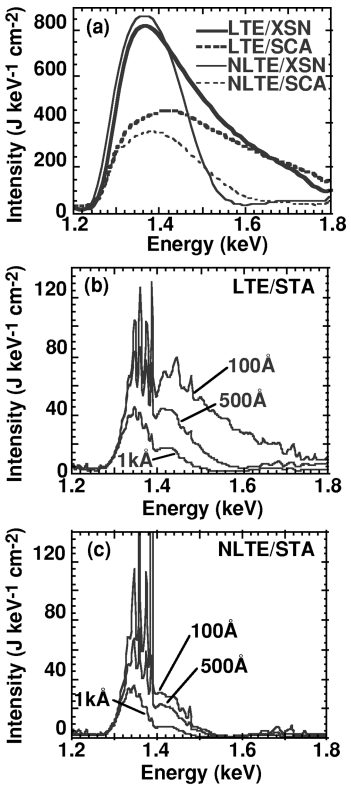

FIG. 6. (a) LASNEX LTE and non-LTE simulations using the average atom XSN model and the simple SCA model; (b) calculated Ge x-ray spectra from LASNEX LTE STA simulations for the three buried layer thicknesses, 100 Å, 500 Å, and 1000 Å CH; (c) calculated x-ray spectra from LASNEX non-LTE STA simulations.

culated spectra presented in this paper are in the same areal units (J keV^{-1} cm^{-2}). Each set of data has been normalized to the LASNEX calculated spectra at the 100 Å CH tamping thickness unless otherwise specified.

The measured spectra for the 1000 Å CH tamping thickness shows the best agreement with the LTE and non-LTE simulations. The individual $3d$-$2p$ lines decrease and the spectrum becomes more featureless. The peak ionization and ionization distributions for both the LTE and non-LTE cases, as reflected in the position and width of the x-ray emission, are in close qualitative agreement with each other and the experiment. The mean ionization distribution time histories for the 1000 Å tamping layer case, shown in Figs. 5(a) and 5(b) for the LTE and non-LTE cases, respectively, were very similar peaking at approximately $+18$ (Si-like) just after the laser pulse and falling off to $+13$ (K-like) at 3 ps. The LTE STA simulations showed a much broader distribution of charge states than the measured data. The non-LTE STA simulations were slightly narrower. This discrepancy may be due to inadequacies in the non-LTE STA or may indicate that the equilibration rates in these dense plasmas are faster than calculated with a simple average atom model (XSN) prescription coupled to small errors in the calculated temperatures. In addition, hot spots (two-dimensional laser intensity inhomogeneities) might enhance the emission from higher charge states and broaden the charge distribution. High-intensity spots may also lead to enhanced oxygenlike and fluorinelike ion populations as the additional structure in the data appears to be consistent with O-like and F-like $3d$-$2p$ lines.

VI. PEAK TEMPERATURE ESTIMATED FROM SPECTRAL LINE INTENSITY RATIOS

For an idealized solid-density plasma in LTE, the ionization distribution is primarily dependent on the electron temperature. The non-LTE ionization distribution is more sensitive to variations in the electron density. The actual ultrashort-pulse laser heated buried layer plasma contains both spatial and temporal gradients and the emission spectra presented in this paper have been integrated over these predicted plasma conditions. The hydrodynamic simulations should account for the range of plasma conditions in the actual experiment and is reflected in the calculated space- and time-integrated spectra. Assuming this is the case, the peak electron temperature for the tracer layer may be deduced by studying the ionization, i.e., studying the emission line intensity ratios as a function of electron temperature.

Detailed simulations were performed for laser intensities ranging from 6×10^{16} W cm^{-2} to 1.5×10^{18} W cm^{-2} and for buried Ge tracer layer depths ranging from 100 Å to 2000 Å of plastic. A flux limiter of 1.0 was used for these simulations. The total space- and time-integrated x-ray emission was calculated for each case applying either LTE or non-LTE ionization STA emission models. Electron temperatures used in the analysis represent peak temperatures in the middle of the 200 Å Ge tracer layer. The Ge L-shell emission is due primarily to $3d$-$2p$ transitions for various ionization charge states with the fluorinelike, neonlike, and sodiumlike transitions occurring between 1.3 and 1.4 keV; oxygenlike, nitrogenlike, and carbonlike transitions in the 1.4–1.5 keV range, and so on. The emissions between 1.6 and 1.7 keV and 1.7–1.8 keV are due to both $3d$-$2p$ transitions in more highly ionized charge states from boronlike, carbonlike, and lithiumlike as well as nd-$2p$ transitions from higher-n excited states. As the electron temperature increases at a constant mass density, the peak ionization shifts towards more highly ionized charge states and is reflected in the calculated spectra. This variation may be used as a crude spectroscopic temperature diagnostic. The non-LTE ionization distribution and L-shell emission spectra are not as strictly temperature dependent as in the LTE case and are slightly more sensitive to variations in the electron density.

The calculated Ge L-shell emissions were integrated over the spectral bands 1.2–1.4 keV labeled A, 1.4–1.5 keV labeled B, 1.6–1.7 keV labeled C, and 1.7–1.8 keV labeled D. The A/B, A/C, and A/D ratios of these integrated spectral bands were plotted as a function of the peak electron temperature at the middle of the Ge tracer layer for each LASNEX LTE and non-LTE simulation as shown in Figs. 7(a), 7(b), and 7(c), respectively. Polynomial curves were fitted to each set of data points (separate curves for the LTE and non-LTE cases) to smooth out anomalous fluctuations from the various simulations. The spectroscopic ratios show monotonic variations decreasing with electron temperature and can be thought of as a coarse measure of the LTE or non-LTE charge state distribution as a function of temperature.

The measured data points were calculated and plotted in Fig. 7 at the peak temperatures (260 eV for 1000 Å and 325 eV for 500 Å) for the middle of the Ge tracer layer from the LASNEX simulations at the 3×10^{17} W cm^{-2}. The tempera-

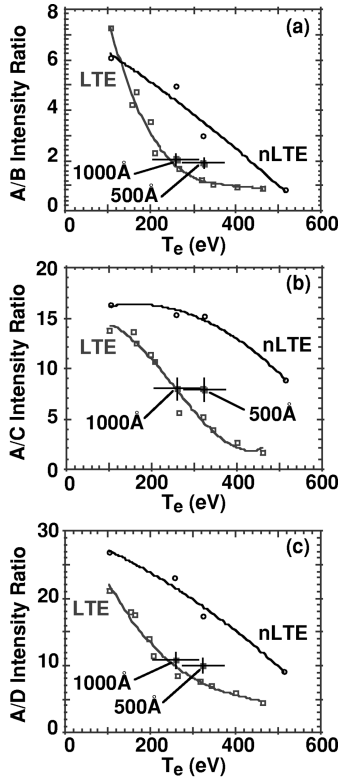

FIG. 7. Calculated LASNEX LTE STA (open squares) and NLTE STA intensity ratios (open circles) for the 500 Å case versus peak electron temperature for (a) A/B, (b) A/C, and (c) A/D, where A is the integrated x-ray fluence between 1200 and 1400 eV, B is the integrated fluence between 1400 and 1500 eV, C is the integrated fluence between 1600 and 1700 eV, and D is the integrated fluence between 1700 and 1800 eV. The measured intensity ratios for the Ge data at the 500 Å and 1000 Å tamping depths are also plotted at the peak temperatures of the midpoint of the Ge tracer layer from the LASNEX simulations. The error bars represent the range in peak temperatures for the Ge tracer layer and an estimated $\pm 10\%$ accuracy in the measured spectral intensity ratio.

ture error bars represent the range in peak temperatures for the Ge tracer layer in the LASNEX simulations. The error bars for the spectral intensity ratios are estimated at $\pm 10\%$ for the A/B ratio and higher for the A/C and A/D ratios. The measured data points lie between the LTE and non-LTE spectral intensity ratio curves. The 1000 Å case should have fewer spatial gradients than the 500 Å case and should be more representative of a homogeneous plasma. A peak LTE plasma temperature of 250 ± 20 eV can be inferred from the comparison of the experimental to calculated spectral ratios and is approximately the same for all three intensity band ratios. The peak non-LTE temperatures fall in the range from 430 ± 50 eV for the A/B ratio to over 500 eV for the other intensity ratios. The non-LTE case should describe the ionization and level kinetics more accurately, but is more sensitive to temperature and density gradients in the problem. The LTE case provides a lower estimated temperature as any departure from LTE conditions in the data would increase the spectral intensity ratios towards non-LTE values for a given peak temperature. Plasma emission in the low-intensity wings of the focal spot will also lower the apparent spectroscopic temperature by weighting the lower ionization emission. Therefore, the electron temperature estimated by

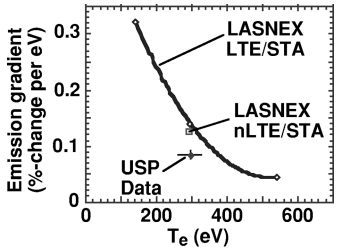

FIG. 8. The 1200–1800 eV x-ray-emission gradient with target depth (between 500 and 1000 Å) is plotted, as the percentage change in emission at 750 Å per angstrom change in CH tamping depth, versus the corresponding peak electron temperature at 750 Å. A fit to the LASNEX LTE STA simulations for different laser intensities shows a nearly linear variation with temperature. The experimental value at 3×10^{17} W cm^{-2} is 0.08%, which corresponds to a temperature of approximately 370 ± 50 eV. The data for the non-LTE simulations are consistent with the LTE values.

comparing measured and calculated spectral line intensity ratios falls between 250 ± 20 eV assuming an ideal case for LTE ionization and 430 ± 50 eV assuming a more realistic non-LTE ionization case.

VII. ESTIMATED TEMPERATURE DETERMINED FROM THE GRADIENT OF THE EMISSION SPECTRA WITH TARGET DEPTH

Another estimate of the temperature can be derived from the variation of the x-ray emission with depth into the target. Because the thermal conductivity is a strong function of temperature (proportional to $T^{5/2}$ for Spitzer conductivity), the temperature gradient is expected to be directly related to the peak temperature at any point in the plasma. [39] Using LASNEX LTE STA simulations, the variation of the total Ge L-shell emission (1200–1800 eV) between the 500 Å and 1000 Å buried layer depths was plotted versus the peak electron temperature for the Ge tracer layer at an equivalent tamping depth of 750 Å. The calculated x-ray-emission gradients were normalized to the average fluence for the 500 Å and 1000 Å buried layer cases, for several different laser intensities. The results represent the percentage change in emission per angstrom of buried depth in plastic and show a decreasing variation with peak electron temperature (at 750 Å) as shown in Fig. 8. The calculated emission gradient has been fit to a second-order polynomial. The normalized non-LTE emission gradient (between 500 Å and 1000 Å at a laser intensity of 3×10^{17} W cm^{-2}) is also shown for comparison. The LTE and non-LTE gradients are very similar since the target hydrodynamics are relatively insensitive to the details of the ionization physics. The variation in x-ray fluence with depth at 750 Å for the measured Ge data (from the 500 Å and 1000 Å data) is 0.08% per angstrom, which corresponds to an electron temperature of 370 ± 50 eV. This emission gradient or ''brightness'' temperature is in fair agreement with the non-LTE spectroscopic line intensity ratio temperature. Uncertainties with this temperature estimate may be due to intensity variations in the focal spot or collisionless absorption not included in these calculations, which increases the apparent peak temperature. Nevertheless, the data are in qualitative agreement with the simulations and are consistent with a peak temperature of 370 ± 50 eV at near

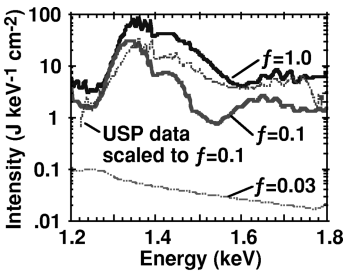

FIG. 9. Ge L-shell spectra calculated from LASNEX LTE STA simulations for the 500 Å CH tamped problem using a flux limiter value of 1.0 at 3×10^{17} W cm^{-2}, 0.1 at 1.5×10^{18} W cm^{-2}, and 0.03 at 1.7×10^{17} W cm^{-2}; the measured Ge L-shell emission spectra for the 500 Å depth have been normalized to the 0.1 flux limiter simulation. (Note the logarithmic intensity scale.)

solid density at 1000 Å beneath the surface of the buried layer target.

VIII. STUDY OF THE THERMAL FLUX LIMITER USED IN HYDRODYNAMIC SIMULATIONS

Flux limited diffusion is commonly used to model thermal transport in laser-produced plasma experiments [17,39] where the thermal energy flux is reduced when energy is transported from the critical surface into a dense plasma. Because of the rapid temporal and spatial variations in short pulse laser produced plasmas, there exists the possibility that the flux inhibition is important in the transport of energy to deeply buried layers in these experiments. A series of LASNEX simulations was conducted for flux limiter values of 0.03, 0.1, and 1.0. The test case was for the 200 Å thick Ge tracer layer tamped by 500 Å CH. The ionization was assumed to be in LTE and the atomic data was provided by the STA opacity data table. Invoking a flux limiter much less than 1.0 significantly changes the hydrodynamics of the plasma. Inhibition of the heat transport forces the local energy density and therefore the electron temperature to extremely high values, creating large temperature gradients. The increased local temperature at the critical surface of the problem (the laser-matter interaction zone) greatly limits the total laser energy absorption into the problem. With the decreased overall absorbed energy and inhibited thermal heat transport from the laser-matter interaction zone, the interior of the target does not get very hot. The Ge tracer layer is less ionized, cooler, and the x-ray emission dramatically drops and does not match the measured data. This occurs for all simulations with the flux limiter other than 1.0.

It might be possible that a collisionless absorption mechanism (not accounted for in the LASNEX simulation) could allow the target to absorb energy despite the high flux limited surface temperature. In order to test this hypothesis, the incident laser flux was artificially increased such that the total absorbed energy was the same as in the flux limiter value 1.0 Ge case at 3×10^{17} W cm^{-2}. The resulting emission spectra calculated by the simulations are shown in Fig. 9. The peak laser flux was increased to 1.5×10^{18} W cm^{-2} for the flux limiter value of 0.1 and 1.7×10^{18} W cm^{-2} for the flux limiter value of 0.03. The simulations are presented on a logarithmic scale so that the 0.03 flux limiter spectra would be included in the plot. The measured spectra at 500 Å CH have been scaled to the 0.1 flux limiter simulation. The calculated x-ray emissions for these simulations clearly disagree with the 1.0 flux limiter case and with the measured data. Because of the inhibited thermal transport, peak temperatures and charge states lag behind the 1.0 flux limiter case and the calculated emission shifts towards lower energies. The differences are greater for more deeply buried layers (a flux limiter value of 0.1) and for all 0.03 flux limter value cases as the heat transport is further inhibited and peak Ge temperatures, ionization, emissivity, and spectrum all shift towards lower values. Therefore, inhibited thermal transport, as invoked by the use of flux limiters much less than 1.0, does not accurately describe the USP generated high-energy, near-solid-density plasmas.

IX. CONCLUSIONS

The x-ray emission from solid-density, germanium tracer layer tamped in plastic and heated by a 130 fs, USP laser pulse at laser intensities of $(2-3)\times10^{17}$ W cm^{-2} have been measured as a function of target depth and compared to detailed hydrodynamic simulations coupled to LTE and non-LTE x-ray spectroscopic emission models generated with the STA opacity code. The measured Ge x-ray data qualitatively agreed with the calculated spectra with peak temperatures ranging from 350–400 eV near the surface ($\approx$200 Å) to 250 eV at 1000 Å. The peak temperature for the Ge at a tamping depth of 1000 Å was estimated by comparing measured and calculated spectral line intensity ratios and falls between 250 ± 20 eV assuming an ideal case for LTE ionization and 430 ± 50 eV assuming a more realistic non-LTE ionization case. Another estimate of the peak electron temperature for the Ge target was determined by comparing the measured x-ray-emission gradient (as a function of tamping depth in plastic between 500 Å and 1000 Å) to calculated emission gradients from LASNEX LTE STA simulations. This emission gradient temperature of 370 ± 50 eV should be less sensitive to the nonequilibrium ionization physics characteristic of the problem.

Additionally, it was found that the thermal energy transport in USP high-energy, near-solid-density plasmas is best modeled by classical heat conduction without any anomalous inhibitions or other modifications using a flux limiter of 1.0. These results qualitatively confirm our calculations of the energy transport, electron temperature, and charge state distribution of dense plasmas produced using ultrashort-pulse, high-intensity lasers. With the continued development of improved lasers, x-ray backlighters, and diagnostics, it should be possible to perform quantitative measurements of the opacity and other radiative properties of plasmas in a region of unprecedented material and energy density using short-pulse laser plasma production.

ACKNOWLEDGMENTS

This work was performed under the auspices of the U.S. Deptartment of Energy by Lawrence Livermore National Laboratory under Contract No. W-7405-Eng-48. The authors also wish to gratefully acknowledge the technical support of J. Bonlie, S. Shiromizu, A. Conder, and A. Ellis and thank A. Osterheld for helpful discussions.

[1] M. M. Murnane, H. C. Kapteyn, and R. W. Falcone, Phys. Rev. Lett. **62**, 155 (1989).
[2] D. Strickland and G. Mourou, Opt. Commun. **56**, 219 (1985).
[3] R. M. More, Z. Zinamon, K. H. Warren, R. Falcone, and M. Murnane, J. Phys. (Paris), Colloq. **61**, C7-43 (1988).
[4] G. Guethlein, M. E. Foord, and D. Price, Phys. Rev. Lett. **77**, 1055 (1996).
[5] K. Nazir, S. J. Rose, A. Djaoui, G. J. Tallents, M. G. Holden, P. A. Norreys, P. Fews, J. Zhang, and F. Failles, Appl. Phys. Lett. **69**, 3686 (1996).
[6] J.-C. Gauthier, J. P. Geindre, P. Audebert, A. Rousse, A. Dos Santos, G. Grillon, A. Antonetti, and R. C. Mancini, Phys. Rev. E **52**, 2963 (1995).
[7] P. Audebert, J. P. Geindre, A. Rouse, F. Fallies, J. C. Gauthier, A. Mysyrowicz, G. Gillon, and A. Antonetti, J. Phys. B **27**, 3303 (1994).
[8] Z. Jiang, J. C. Kieffer, J. P. Matte, M. Chaker, O. Peyrusse, D. Gilles, G. Korn, A. Maksimchuk, S. Coe, and G. Mourou, Phys. Plasmas **2**, 1702 (1995).
[9] J. C. Kieffer, M. Chaker, C. Y. Cote, Y. Beaudoin, H. Pepin, C. Y. Chien, S. Coe, and G. Mourou, Appl. Opt. **32**, 4247 (1993).
[10] J. C. Kieffer, M. Chaker, J. P. Matte, H. Pepin, C. Y. Cote, Y. Beaudoin, T. W. Johnson, C. Y. Chien, S. Coe, G. Mourou, and O. Peyrusse, Phys. Fluids B **5**, 2676 (1993).
[11] H. Chen, B. Soom, B. Yaakobi, S. Uchida, and D. D. Meyerhofer, Phys. Rev. Lett. **70**, 3431 (1993).
[12] U. Teubner, C. Wulker, W. Theobald, and E. Forster, Phys. Plasmas **2**, 972 (1995).
[13] A. Zigler, P. G. Burkhalter, D. J. Nagel, M. D. Rosen, K. Boyer, G. Gibson, T. S. Luk, A. McPherson, and C. K. Rhodes, Appl. Phys. Lett. **59**, 534 (1991).
[14] A. Zigler, P. G. Burkhalter, D. J. Nagel, K. Boyer, T. S. Luk, A. McPherson, J. C. Solem, and C. K. Rhodes, Appl. Phys. Lett. **59**, 777 (1991).
[15] G. B. Zimmerman and W. L. Kruer, Comments Plasma Phys. Control. Fusion **2**, 51 (1975).
[16] G. B. Zimmerman and R. M. More, Lawrence Livermore National Laboratory Annual Report No. UCRL-55021-80, pp. 3–71, 1980 (unpublished).
[17] J. A. Harte, W. E. Alley, D. S. Bailey, J. L. Eddleman, and G. B. Zimmerman, Lawrence Livermore National Laboratory Report No. UCRL-LR-105821-96-4, p. 150, 1996 (unpublished).
[18] A. Bar-Shalom, J. Oreg, W. Goldstein, D. Shvarts, and A. Zigler, Phys. Rev. A **40**, 3183 (1989).
[19] A. Bar-Shalom, J. Oreg, and W. Goldstein, Phys. Rev. E **51**, 4882 (1995).
[20] M. Busquet, Phys. Fluids B **5**, 4191 (1993).
[21] A. Bar-Shalom, J. Oreg, and M. Klapisch, J. Quant. Spectrosc. Radiat. Transf. **58**, 427 (1997).
[22] M. Klapisch and A. Bar-Shalom, J. Quant. Spectrosc. Radiat. Transf. **58**, 687 (1997).
[23] B. K. F. Young, B. G. Wilson, G. B. Zimmerman, D. F. Price, and R. E. Stewart, J. Quant. Spectrosc. Radiat. Transf. **58**, 991 (1997).
[24] D. F. Price, R. M. More, R. S. Walling, G. Guethlein, R. L. Shepherd, R. E. Stewart, and W. E. White, Phys. Rev. Lett. **75**, 252 (1995).
[25] A. Sullivan, J. Bonlie, D. F. Price, and W. E. White, Opt. Lett. **21**, 603 (1996).
[26] J. D. Bonlie, W. E. White, D. F. Price, and D. H. Reitze, Proc. SPIE **2116**, 312 (1994).
[27] A. D. Conder, J. Dunn, and B. K. F. Young, Rev. Sci. Instrum. **66**, 709 (1995).
[28] J. Dunn, B. K. F. Young, A. D. Conder, and R. E. Stewart, Proc. SPIE **2654**, 119 (1996).
[29] B. L. Henke, P. Lee, T. J. Tanaka, R. L. Shimabukuro, and B. K. Fujikawa, At. Data Nucl. Data Tables **27**, 1 (1982).
[30] B. L. Henke, J. P. Knauer, and K. Premaratne, J. Appl. Phys. **52**, 1509 (1981).
[31] A. Burek, Space Sci. Instrum. **2**, 53 (1976).
[32] J. Dunn, H. A. Baldis, G. D. Enright, B. La Fontaine, D. M. Villeneuve, and J. C. Kieffer (unpublished).
[33] A. L. Osterheld, J. Dunn, B. K. F. Young, M. Foord, R. W. Lee, W. H. Goldstein, R. E. Stewart, A. Ya. Faenov, I. Skobelev, S. Khakhalin, S. Pikuz, T. Shelkovenko, and V. Romanova (unpublished).
[34] W. H. Goldstein, R. S. Walling, J. Bailey, M. H. Chen, R. Fortner, M. Klapisch, T. Phillips, and R. E. Stewart, Phys. Rev. Lett. **58**, 2300 (1987).
[35] J. Bailey, R. E. Stewart, J. D. Kilkenny, R. S. Walling, T. W. Phillips, R. J. Fortner, and R. W. Lee, J. Phys. B **19**, 2639 (1986).
[36] R. M. More, K. H. Warren, D. A. Young, and G. B. Zimmerman, Phys. Fluids **31**, 3059 (1988).
[37] Hard x-ray measurements for similar targets heated at laser intensities above 5×10^{18} W cm^{-2} were in the range of 10^{-4} of the laser energy on target for x-ray energies above 10 keV and 10^{-6} for x-ray energies between 30 keV and 1 MeV. The hard x-ray generation will be much less for lower laser intensities.
[38] Y. T. Lee and R. M. More, Phys. Fluids **27**, 1273 (1984).
[39] C. E. Max, in *Physics of Laser Fusion*, Proceedings of the Les Houches Summer School of Theoretical Physics, edited by R. Balian and J. C. Adam, (North-Holland, Amsterdam, 1981), p. 301.
[40] W. A. Lokke and W. H. Grasberger, Lawrence Livermore National Laboratory Report No. UCRL-52276, 1977 (unpublished).
[41] G. Pollak, Los Alamos National Laboratory Report No. LA-UR-90-2423, 1990 (unpublished).
[42] G. B. Zimmerman (private communication).